Available online at www.sciencedirect.com
SCIENCE DIRECT
ELSEVIER
ISPRS Journal of Photogrammetry & Remote Sensing 60 (2006) 100–112
PHOTOGRAMMETRY & REMOTE SENSING
www.elsevier.com/locate/isprsjprs

Gaussian decomposition and calibration of a novel small-footprint full-waveform digitising airborne laser scanner

Wolfgang Wagner [a,*], Andreas Ullrich [b], Vesna Ducic [a], Thomas Melzer [a], Nick Studnicka [b]

[a] *Christian Doppler Laboratory for Spatial Data from Laser Scanning and Remote Sensing, Vienna University of Technology, Gusshausstrasse 27-29, 1040 Vienna, Austria*
[b] *Riegl Research GmbH, 3580 Horn, Austria*

Received 4 October 2005; received in revised form 7 December 2005; accepted 9 December 2005
Available online 27 January 2006

Abstract

In this study we use a technique referred to as Gaussian decomposition for processing and calibrating data acquired with a novel small-footprint airborne laser scanner that digitises the complete waveform of the laser pulses scattered back from the Earth's surface. This paper presents the theoretical basis for modelling the waveform as a series of Gaussian pulses. In this way the range, amplitude, and width are provided for each pulse. Using external reference targets it is also possible to calibrate the data. The calibration equation takes into account the range, the amplitude, and pulse width and provides estimates of the backscatter cross-section of each target. The applicability of this technique is demonstrated based on RIEGL LMS-Q560 data acquired over the city of Vienna.

Keywords: Laser scanning; Lidar; Digitisation; Calibration; Retrieval

1. Introduction

Airborne laser scanning (ALS), also referred to as lidar or laser radar, is an active remote sensing technique where a laser emits short infrared pulses towards the Earth's surface and a photodiode records the back-scattered echo. A timer measures the round-trip time of the laser pulse that allows calculating the range (distance) between the laser scanner and the object that generated the backscattered echo. Thereby, information about the geometric structure of the Earth's surface is obtained.

In the last ten years major advances have been made in environmental and other non-military ALS applications. These advances have been driven to a large extent by increasing technological capabilities of ALS systems (sampling density, multiple pulses, positional accuracy, etc.). Remarkably, much of the technological innovation was borne by commercial ALS manufacturers and service providers, who entered the field in the mid-1990s (Flood, 2001). Nowadays, ALS is used routinely for topographic mapping and is considered to hold a large potential in a range of other applications such as forestry, 3D city modelling or power line detection.

A major challenge for algorithm development is that, so far, most ALS systems have provided only the coordinates of scattering objects. The task is then to

* Corresponding author.
E-mail address: ww@ipf.tuwien.ac.at (W. Wagner).

0924-2716/$ - see front matter
doi:10.1016/j.isprsjprs.2005.12.001

derive useful object representations from the irregular 3D point cloud (Axelsson, 1999). This normally involves a classification of the 3D data into different object classes. For example, in order to derive digital terrain models (DTMs), laser pulses reflected by the ground surface must be distinguished from non-terrain points. This task can be achieved using various filtering techniques that classify the point cloud into terrain and off-terrain points just based on the spatial relationship of the 3D data (Sithole and Vosselman, 2004). Once the terrain hits are correctly classified the generation of a DTM is straightforward.

Methods for ALS data processing could be much improved if ALS systems would measure, in addition to the range, further physical observables that can be used for object classification. Even though some advanced ALS systems already measure the intensity of each echo, only few studies have yet used these data. Nevertheless, first classification results are promising (e.g., Rottensteiner et al., 2005). In addition, experimental ALS systems developed by the National Aeronautics and Space Administration (NASA) have demonstrated the value of recording the complete waveform of the backscattered echo for vegetation analysis. In this paper we present the RIEGL airborne laser scanner LMS-Q560, which is one of the first commercial full-waveform digitising laser scanners. Based on theoretical considerations and first airborne measurements acquired over the city of Vienna, we demonstrate that recording the full waveform is necessary to depict the physical measurement process in its entire complexity. The contributions of this paper to the literature are:

- to provide a theory for Gaussian pulse formation as a basis for Gaussian decomposition and calibration of small-footprint full-waveform ALS (Section 2);
- to be a technical reference document for the RIEGL LMS-Q560 (Section 3);
- to discuss the applicability of the Gaussian decomposition method to small-footprint full-waveform ALS data (Sections 4 and 5).

2. Theory

2.1. Radar equation

Airborne laser scanning utilizes a measurement principle firstly introduced in radar remote sensing. The fundamental relation to explain the signal strength in both techniques is the radar equation. The radar equation is used for system design and calibration and is treated in many text books (Ulaby et al., 1982; Jelalian, 1992). However, we derive it here step by step because we use a formulation particularly adapted to ALS and because it provides the basis for our further considerations. The main parameters involved in the radar equation are illustrated in Fig. 1. The laser transmits a narrow beam towards the scatterer. The footprint area of the beam at the scatterer is approximately given by

$$A_{\text{laser}} = \frac{\pi R^2 \beta_t^2}{4} \tag{1}$$

where R is the range and β_t is the transmitter beamwidth. Therefore the power density S_s of the laser beam at the scatterer is:

$$S_s = \frac{4P_t}{\pi R^2 \beta_t^2}. \tag{2}$$

where P_t is the transmitted power. This equation describes the reduction in power density associated with the spreading of the laser beam. To obtain the total power intercepted by the scatterer the power density must be multiplied by the effective receiving area of the scatterer. Since the laser wavelength is always much smaller than the size of the scattering elements (e.g., leaf, roof) the effective area of collision is simply the projected area of the scatterer. Some of the power received by the scatterer is absorbed, the rest is reradiated (=scattered) in various directions. Thus the scattered power P_s is

$$P_s = S_s \rho A_s = \frac{4P_t}{\pi R^2 \beta_t^2} \rho A_s \tag{3}$$

where ρ is the reflectivity and A_s is the receiving area of the scatterer. The reradiation pattern is in general complex, but for simplicity let us assume that the incoming radiation is scattered uniformly into a cone of solid angle Ω (Fig. 2). If this cone does not overlap with the field of view of the receiver optics then no return signal is registered, i.e., the laser pulse is scattered away from the sensor. If it overlaps, the power density S_r at the receiver is

$$S_r = \frac{P_s}{\Omega R^2} = \frac{4P_t}{\pi R^2 \beta_t^2} \rho A_s \frac{1}{\Omega R^2} \tag{4}$$

The power entering the receiver is

$$P_r = S_r \frac{\pi D_r^2}{4} = \frac{4P_t}{\pi R^2 \beta_t^2} \rho A_s \frac{1}{\Omega R^2} \frac{\pi D_r^2}{4} \tag{5}$$

where D_r is the aperture diameter of the receiver optics. When we separate sensor and target parameters

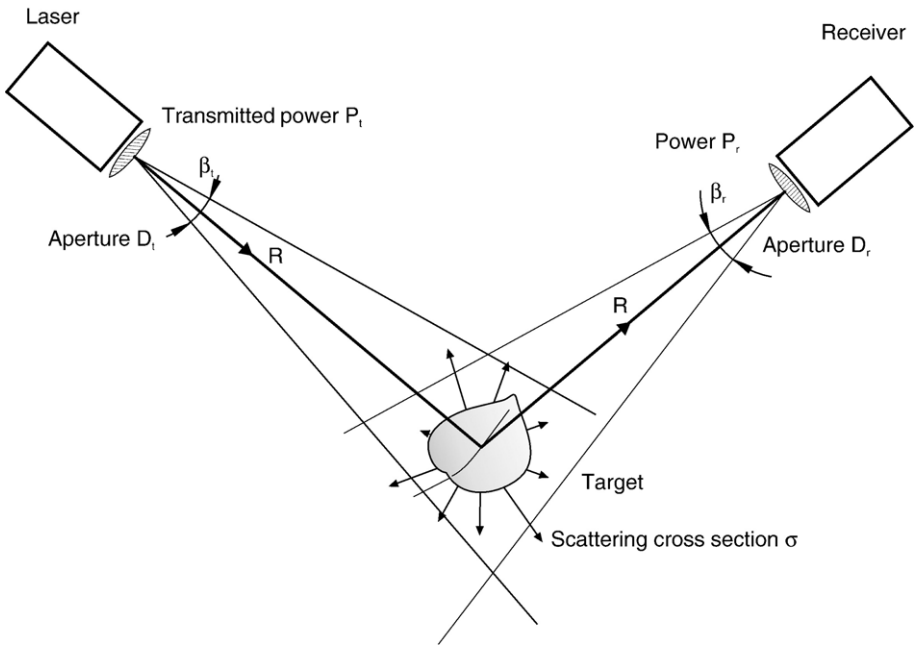

Fig. 1. Geometry and parameters involved in the radar equation. Laser scanners are monostatic, that is the transmitter and receiver are side by side at the same location. In this figure transmitter and receiver are drawn at different locations for clarity.

we arrive at following formulation of the radar equation:

$$P_r = \frac{P_t D_r^2}{4\pi R^4 \beta_t^2}\sigma. \quad (6)$$

All target parameters were combined into one parameter, the so-called backscatter cross-section σ :

$$\sigma = \frac{4\pi}{\Omega}\rho A_s. \quad (7)$$

This relation shows that the backscattering characteristics of a target depend on its size, its reflectivity, and the directionality of scattering. The superimposed effects of target size, reflectivity, and directionality are the reason why Katzenbeisser and Kurz (2004) remark that ALS intensity information may not be as straight forward to use for classification purposes as reflectivity values recorded with passive imaging sensors, particularly if multiple targets are recorded. On the other hand, ALS intensity values are not obscured by shadow effects and do not suffer from changing illumination conditions (position of the sun with respect of the sensor, clouds, etc.).

2.2. Waveform

Let us now consider the temporal shape of the signal, which is commonly referred to as waveform. For point scatterers or non-tilted, flat surfaces the received signal

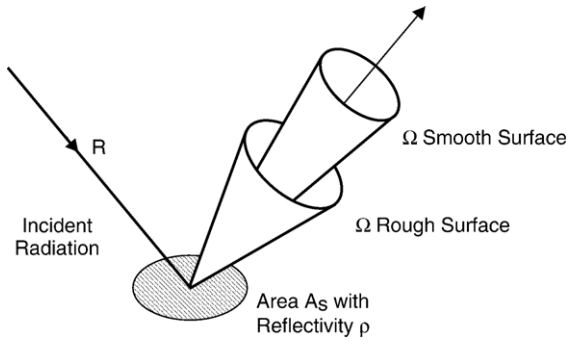

Fig. 2. Parameters affecting the cross-section of a target.

is simply a delayed and attenuated replica of the transmitted signal:

$$P_r(t) = \frac{D_r^2}{4\pi R^4 \beta_t^2} \cdot P_t\left(t - \frac{2R}{v_g}\right) \cdot \sigma \quad (8)$$

where t is the time. The time delay is equal to $t' = 2R/v_g$ where v_g is the group velocity of the laser pulse in the atmosphere. Because of this latter relation the variables time and range can be used interchangeably.

For spatially distributed targets the return signal is the superposition of echoes from scatterers at different ranges/times. Scatterers produce distinct echoes if separated by distances larger than the range resolution of the ALS system. The range resolution is equal to $v_g\tau/2$, where τ is the pulse duration of the ALS system. If the scatterers are clustered at smaller distances then their effect is to smear out the original pulse. Let us describe such a cluster of scatterers by its mean range position R_i, its spatial extent $[R_i - \Delta R, R_i + \Delta R]$, and its differential backscatter cross-section $\sigma_i(R)$, which is defined as the cross-section per range interval dR. The echo from this cluster is

$$P_{r,i}(t) = \frac{D_r^2}{4\pi\beta_t^2} \int_{R_i-\Delta R}^{R_i+\Delta R} \frac{1}{R^4} \cdot P_t\left(t - \frac{2R}{v_g}\right) \cdot \sigma_i(R)\mathrm{d}R. \quad (9)$$

We can see that the echo pulse is the result of a convolution of the transmitted pulse and the differential cross-section, multiplied by the term R^{-4}. For relatively long clusters, where pulse spreading is important over their length, this latter term cannot be neglected. However, in situations where $\Delta R \ll R$ the following zero-order approximation can be made:

$$\begin{aligned} P_{r,i}(t) &\approx \frac{D_r^2}{4\pi R_i^4 \beta_t^2} \int_{R_i-\Delta R}^{R_i+\Delta R} P_t\left(t - \frac{2R}{v_g}\right) \cdot \sigma_i(R)\mathrm{d}R \\ &= \frac{D_r^2}{4\pi R_i^4 \beta_t^2} P_t(t) * \sigma_i'(t) \end{aligned} \quad (10)$$

where * is the convolution operator and $\sigma_i'(t) = \sigma_i(R)$. In ALS this appears to be a useful working assumption because the flight altitude is in general much larger than the range resolution and because of the small laser footprint size. For the LMS-Q560 the range resolution is 0.6 m, i.e., scatterers that are further apart produce distinct echoes. If there are N such distinct targets within the travel path of the laser pulse then the recorded waveform is simply the sum of all echoes:

$$P_r(t) = \sum_{i=1}^{N} \frac{D_r^2}{4\pi R_i^4 \beta_t^2} P_t(t) * \sigma_i'(t) \quad (11)$$

Please note that for multiple echoes the scatterers generating the second and higher number pulses may be partly shaded by the scatterers closer to the sensor. Since these shaded areas do not contribute to the return signal, $\sigma_i'(t)$ is an "apparent" cross-section that represents only illuminated areas within each range interval.

2.3. System waveform

So far we have neglected the impact of the receiver on the waveform. This effect can be accounted for by introducing the receiver impulse function $\Gamma(t)$:

$$P_r(t) = \sum_{i=1}^{N} \frac{D_r^2}{4\pi R_i^4 \beta_t^2} P_t(t) * \sigma_i'(t) * \Gamma(t) \quad (12)$$

In practice, $P_t(t)$ and $\Gamma(t)$ cannot be easily determined independently. Therefore it is advantageous to rewrite the convolution term by making use of the commutative property of the convolution operator:

$$\begin{aligned} P_t(t) * \sigma_i'(t) * \Gamma(t) &= P_t(t) * \Gamma(t) * \sigma_i'(t) \\ &= S(t) * \sigma_i'(t) \end{aligned} \quad (13)$$

where we introduce the system waveform $S(t)$ of the laser scanner, defined as the convolution of the transmitted pulse and the receiver response function. It can be measured experimentally and is shown in Fig. 3 for the Riegl LMS-Q560. It can be seen that it is well described by a Gaussian function:

$$S(t) = \hat{S} \mathrm{e}^{-\frac{t^2}{2s_s^2}} \quad (14)$$

where $\hat{S}$ is the amplitude and s_s the standard deviation.

2.4. Gaussian scatterers

In order to come to an analytical waveform solution, let us assume that the scattering properties of a cluster of scatterers can be described by a Gaussian function:

$$\sigma_i'(t) = \hat{\sigma}_i \mathrm{e}^{-\frac{(t-t_i)^2}{2s_i^2}} \quad (15)$$

where $\hat{\sigma}$ is the amplitude and s_i the standard deviation of the cluster i. Its position is specified by t_i. The total cross-section of such a Gaussian target is

$$\sigma_i = \int_{-\infty}^{\infty} \hat{\sigma}_i \mathrm{e}^{-\frac{(t-t_i)^2}{2s_i^2}} \mathrm{d}t = \sqrt{2\pi} s_i \hat{\sigma}_i. \quad (16)$$

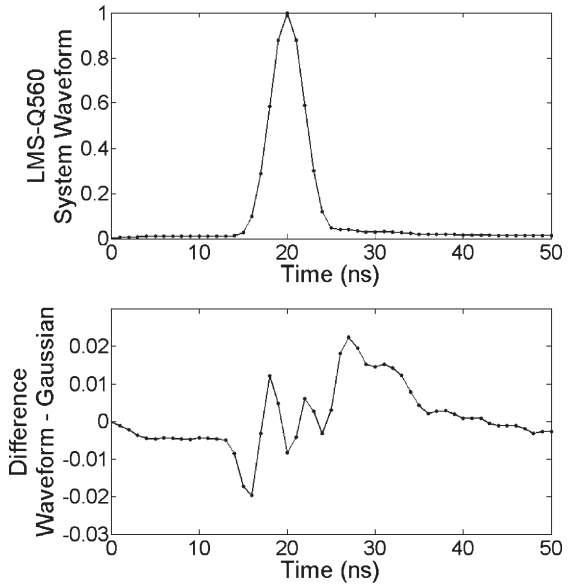

Fig. 3. LMS-Q560 waveform displayed in relative units. The bottom figure shows the deviations to a Gaussian model.

The convolution of two Gaussian curves gives again a Gaussian function, so that we obtain:

$$S(t)*\sigma_i'(t) = \sqrt{2\pi}\hat{S}\hat{\sigma}_i \frac{s_s s_i}{\sqrt{s_s^2+s_i^2}} e^{-\frac{(t-t_i)^2}{2(s_s^2+s_i^2)}} = \hat{S}\sigma_i \frac{s_s}{\sqrt{s_s^2+s_i^2}} e^{-\frac{(t-t_i)^2}{2(s_s^2+s_i^2)}}. \quad (17)$$

We substitute the right hand term of Eq. (17) into Eq. (12) and get as our final result:

$$P_r(t) = \sum_{i=1}^{N} \hat{P}_i e^{-\frac{(t-t_i)^2}{2s_{p,i}^2}} \quad (18)$$

where t_i is the round-trip time, $s_{p,i}$ the standard deviation of the echo pulse, and $\hat{P}_i$ the amplitude of cluster i:

$$s_{p,i} = \sqrt{s_s^2+s_i^2}, \quad (19)$$

$$\hat{P}_i = \frac{D_r^2}{4\pi R_i^4 \beta_t^2}\hat{S}\sigma_i \frac{s_s}{s_{p,i}}. \quad (20)$$

The comparison of Eq. (20) with Eq. (6) shows that for Gaussian scatterers the form of the radar equation is preserved. The only differences are that P_t is replaced by the term $\hat{S}s_s$ and P_r by $\hat{P}_i s_{p,i}$, which is an expression of the fact that the pulse energy is proportional to the area below the pulse.

2.5. Calibration

In radar remote sensing the radar equation is used to convert the measured receiver power into the radar cross-section. This is referred to as calibration and is necessary when measurements of different instruments and models are to be compared. Calibration is generally achieved by passing a sample of the transmitted signal through the receiver and by monitoring the signal from standard targets (Ulaby et al., 1982). Also in ALS reference targets can be used for calibration. Kaasalainen et al. (2005) suggest using portable brightness targets with Lambertian (diffuse) reflectance characteristics and known reflectance values. For the calibration of the LMS-Q560 with an extended reference target we can use Eq. (20). We need to consider that additional power losses may occur in the instrument and in the atmosphere:

$$\hat{P}_i = \eta_{sys}\eta_{atm}\frac{D_r^2}{4\pi R_i^4 \beta_t^2}\hat{S}\sigma_i \frac{s_s}{s_{p,i}} \quad (21)$$

where η_{sys} is the system transmission factor and η_{atm} is the atmospheric transmission factor. Inverting this equation and separating constant from variable terms yields the calibration equation:

$$\sigma_i = C_{cal} R_i^4 \hat{P}_i s_{p,i} \quad (22)$$

where C_{cal} is the calibration constant:

$$C_{cal} = \frac{4\pi\beta_t^2}{\eta_{sys}\eta_{atm}D_r^2\hat{S}s_s}. \quad (23)$$

Here we assumed a high stability of the laser pulse power and constant atmospheric conditions throughout the acquisition area. Should the intensity of the transmitted laser pulse and its pulse width vary over time then the term $\hat{S}s_s$ could simply be moved from Eq. (23) to (22). Effects of the atmosphere, e.g., due to variable water vapour or aerosol concentrations in the acquisition area, would be more difficult to correct due to the lack of suitable reference data. More research is needed to quantify their impact upon ALS data.

3. Sensor

A large variety of laser scanning systems has been developed, ranging from inexpensive, portable airborne systems to technologically advanced spaceborne systems such as the Geoscience Laser Altimeter System (GLAS) onboard the ICESat satellite (Zwally et al., 2002). Important technical parameters to characterise the physical properties of laser scanner systems are the laser wavelength (μm), pulse duration (ns), pulse energy

(μJ), pulse rate (kHz), beamwidth (mrad), scan angle (deg), scan rate (Hz), flying height (m), and size (m) of laser footprint on ground (Baltsavias, 1999). In addition, the design of the receiver–recording unit is important, in particular if the system records discrete pulses (with or without intensity and pulse width measurements) or if it is capable of digitising the complete backscattered waveform. In the first case analog detectors are used to derive discrete, time-stamped trigger pulses from the received signal in real time during the acquisition process. For example, in the case of the Mars Orbiter Laser Altimeter (MOLA), which was used for global topographic mapping of Mars, an analog filter-threshold crossing approach was chosen to determine the range (Abshire et al., 2000). In addition, the MOLA receiver also measured the pulse width and area of the filtered echo pulse at the threshold crossings. Unfortunately, in the case of commercial ALS systems detailed information concerning the analog detection method is normally missing, even though different detection methods may yield quite different range estimates (Wagner et al., 2004).

Digitising and recording the complete backscattered waveform during the acquisition for later post-processing has the advantages that algorithms can be adjusted to tasks, intermediate results are respected, and neighbourhood relations of pulses can be considered (Jutzi and Stilla, 2003). The technical feasibility has been demonstrated by large-footprint airborne systems developed by NASA in the 1990s, namely the Scanning Lidar Imager of Canopies by Echo Recover (SLICER) and the Laser Vegetation Imaging Sensor (LVIS) (Blair et al., 1994, 1999). These experimental airborne systems have been used to study the large-footprint waveform of different land cover classes, e.g., broadleaf forest (Harding et al., 2001) and tropical forest (Hofton et al., 2002). The first satellite instrument capable of digitising the backscattered waveform is GLAS, launched onboard of ICESat in 2003. ICESat, as the name suggests, is primarily designed for measuring the elevations of the ice sheets but also provides waveform data over land, oceans, and sea-ice. Recently, three commercial airborne systems have become available, namely the RIEGL LMS-Q560 (www.riegl.co.at), the TopEye Mark II system (www.topeye.com), and Optech's ALTM 3100 system (www.optech.on.ca) (Persson et al., 2005).

The RIEGL LMS-Q560 became operational in 2004 (Hug et al., 2004). Its specifications are compared to LVIS, GLAS, ALTM 3100 and Mark II in Table 1. Table 2 provides additional technical details. The most notable differences between the three systems relate to the operations altitude and consequently the required laser pulse energy and the size of the receiver aperture. Small-footprint ALS systems generally have moderate pulse energy levels and high firing rates, whereas the high-altitude airborne LVIS and the spaceborne GLAS instrument have a high pulse energy and a low firing rate. The satellite-based GLAS instrument additionally requires a very narrow beamwidth to achieve a moderate laser footprint size on the Earth's surface. On the other hand, the width of the transmitted pulse and the sampling interval for the digitisation of the echo waveform are very similar for all three systems, namely 4–10 ns pulse width at half maximum and 1–2 ns sampling interval.

The LMS-Q560 records all echo pulses and a fraction of the transmitted pulse. This is illustrated in Fig. 4 where the top most line depicts the analog signals: the first (left most) pulse relates to a fraction of the laser transmitter pulse, and the following pulses correspond to the reflections, e.g., by the branches of a tree and by the ground. This analog echo signal is sampled at 1 ns intervals (middle line) and is subsequently AD converted, resulting in a digital data stream (bottom line).

Table 1
Specifications of five waveform-digitising laser scanner systems: Laser Vegetation Imaging Sensor (LVIS) (Blair et al., 1999), Geoscience Laser Altimeter System (GLAS) (http://icesat.gsfc.nasa.gov/, Zwally et al., 2002), Optech ALTM 3100 with Intelligent Waveform Digitiser (http://www.optech.ca/), TopEye Mark II (http://www.topeye.com/ and Persson et al., 2005) and RIEGL LMS-Q560 (http://www.riegl.com/)

Sensor	LVIS	GLAS	ALTM 3100	Mark II	LMS-Q560
Operating altitude	<10 km	600 km	<2500 m *	<1000 m	<1500 m
Wavelength	1.06 μm	1.06 μm	1.06 μm	1.06 μm	1.5 μm
Pulse width at half maximum	10 ns	6 ns	8 ns	4 ns	4 ns
Pulse energy	5 mJ	75 mJ	<200 μJ	Not available	8 μJ
Pulse firing rate	100–500 Hz	40 Hz	<50 kHz *	<50 kHz	<100 kHz
Laser beamwidth	8 mrad	110 μrad	0.3 or 0.8 mrad	1 mrad	0.5 mrad
Scan angle range	±7°	Fixed at 0°	Up to ±25°	Fixed 20° or 14°	±22.5°
Footprint size	40 m @ 5 km	66 m	0.3 or 0.8 m@ 1 km	1 m @ 1 km	0.5 m @ 1 km
Digitiser	2 ns	1 ns	1 ns	1 ns	1 ns

*Limit with intelligent waveform digitiser.

Table 2
Technical specifications of RIEGL LMS-Q560

Parameter	Value
Measurement range	30–1500 m at target reflectivity of 80% 30–850 m at target reflectivity of 20%
Ranging accuracy	20 mm
Multi-target range resolution	0.6 m
Measurement rate	100 000 measurements/s (burst rate) up to 66 000 measurements/s (average)
Scan range	45°(up to 60°)
Scan speed	Up to 160 lines/s
Digitiser bits	16
Maximum number of samples per laser shot	<800 @ pulse firing rate 100 kHz
Synchronization	GPS PPS and serial IF
Time stamping	resolution 1 μs, unambiguous range>1 week
Size/weight	560×200×217 mm /20 kg
Laser safety	Laser class 1/wavelength near infrared

Addendum to Table 1.

After pre-processing the data stream for data reduction, the sample data are stored in the RIEGL Data Recorder DR560 together with scan angle and a high-accuracy GPS time stamp.

The LMS-Q560 system waveform is very similar to an ideal Gaussian function. This is illustrated in Fig. 3 where the waveform is compared to a fitted Gaussian model. The difference plot shows that the ascending flank of the pulse is somewhat steeper than of the Gaussian model. Also, we can observe a rather long, but weak tail of the pulse. These differences are less than ±2% of the signal amplitude. This demonstrates that a Gaussian model is nevertheless well suited for modeling LMS-Q560 data.

4. Method

The principal parameter of interest is the backscatter cross-section. It provides information about the range and scattering properties of the targets. Because the system waveform $S(t)$ is known the cross-section profile can be directly derived from the registered waveform $P_r(t)$ using deconvolution techniques. The so derived profiles can be mapped into a 3D data space for further analysis. Another approach is to model the waveform as a series of Gaussian distribution functions, as demonstrated for LVIS by Hofton et al. (2000) and for the TopEye Mark II system by Persson et al. (2005). This Gaussian decomposition method goes one step further than deconvolution methods because it provides estimates of the location and scattering properties of the targets within the travel path of the laser beam, i.e., the number of pulses N and for each pulse the time t_i, the amplitude $\hat{P}_i$, and the pulse width $s_{p,i}$ as specified in Eq. (18). This is illustrated in Fig. 5 that shows a measured waveform from a forested area, the fitted echo pulses and the corresponding cross-section profile. As a result, an interpretation of the data is obtained and the data volume is much reduced.

As was shown in the theory part of the paper, the implicit assumption of Gaussian decomposition is that the cross-section profile can be represented by a series of Gaussian functions, whereby each pulse represents a cluster of scatterers situated too closely to be resolved

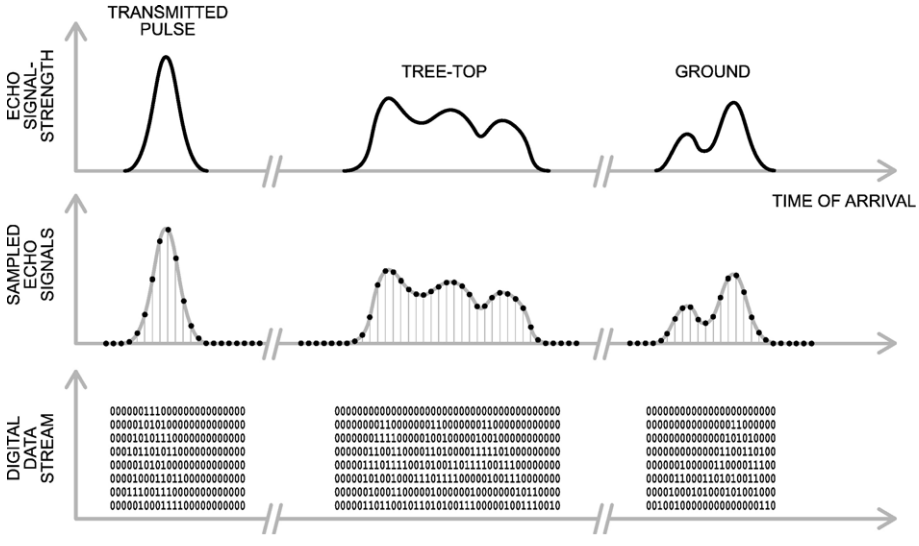

Fig. 4. Principle of waveform digitisation in LMS-Q560. The transmitted and received laser pulses are digitised and stored in blocks.

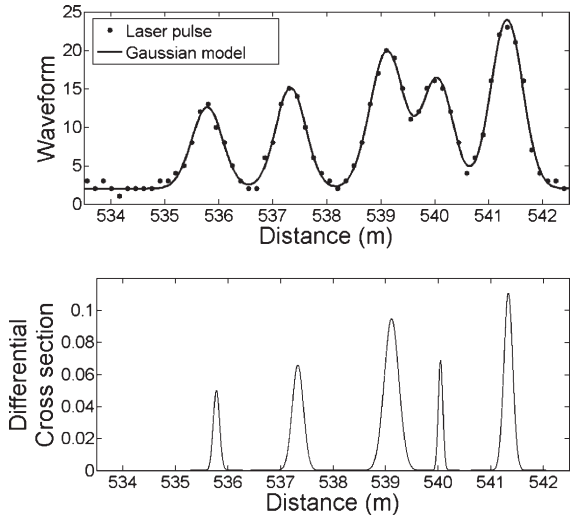

Fig. 5. Example of a measured versus the modelled waveform (top). The bottom figure shows the corresponding cross-section profile in m^2 m^{-1}.

by the range resolution of the ALS system. However, given the complex form and reflectivity properties of natural and man-made objects and considering intensity variations of the laser beam over its footprint, one has to expect that this assumption is, in a strict sense, often not correct. On the other hand, determination of the scattering cross-section from the observed waveform is an inherently ill-posed problem, i.e., we cannot hope to obtain a unique solution unless we impose additional constraints based on a priori knowledge or assumptions. In the absence of complete a priori knowledge (e.g., the true parametric form of the cross-section), the choice of the solution is normally governed by Occam's Razor, which states that given multiple, competing hypotheses explaining the observations equally well, we should choose the simplest one (Cherkassky and Mulier, 1998). For example, deconvolution techniques typically employ some form of regularization that penalizes solutions with high-frequency components (Bennia and Sedki, 1990), and thus prefers smoother, simpler explanations over more complex ones. From this point of view, the assumption that the scattering cross-section is a superposition of Gaussians is just another example of constraining the class of possible solutions in favour of simpler ones. As a matter of fact, there exists a close relationship between regularization and the reconstruction of a signal in terms of a superposition of Gaussians (Girosi et al., 1995).

Therefore, from a theoretical point of view, we are perfectly justified to make the assumption of Gaussian decomposition as long as there is no evidence as to the contrary. This evidence will have to be based on the quality of the explanation (or reconstruction) of the observed waveform in terms of the fitted model. The root mean square error (RMSE) is one possible candidate among other criteria, which we shall discuss later. From a practical point of view, our implementation of Gaussian decomposition offers the advantage that the solution can be obtained in closed form and that the computed parameters have a direct physical interpretation.

We tested the applicability of the Gaussian decomposition theory to LMS-Q560 data by performing an unconstrained fit to the measured waveforms and by calculating the root mean square error between the measured and modelled waveform. The Gaussian decomposition of a waveform comprising N pulses is determined by $3N$ unknown parameters (Eq. (18)), which are obtained by solving a non-linear least-squares problem. Non-linear optimization techniques, like the Levenberg–Marquardt method, depend on a realistic set of initial parameter estimates in order to limit the likelihood of the least-squares-derived solution ending up in a local minimum. Our method estimates the number of Gaussian components and their respective amplitudes and positions by applying two "traditional" pulse detection methods, namely the centre of gravity and zero-crossing of the first derivative (Wagner et al., 2004). Only if these to detectors agreed (within a given tolerance), the final fit was computed. Disagreement between the pulse detectors does not necessarily imply that the assumption of Gaussian decomposition does not hold in that particular case, but it typically indicates the presence of fine (high-frequent) structures in the waveform—typically due to close singular scatterers whose distance is below the range resolution of the scanner—which cannot easily be resolved. We illustrate this in Fig. 6 where we have two closely located Gaussian scatterers, e.g., two branches of a tree. As long as two scatterers are further apart than the range resolution of the ALS system they appear as individual scatters in the measured waveform. When the two scatterers are at a distance comparable to or smaller than the range resolution then they form a scattering cluster. The recorded waveform may still produce two visible peaks, but in general, the two scatterers will be merged into one mode. Also, situations where one fitted pulse was negative or the fitting procedure did not find a solution at all were considered as problematic.

The LMS-Q560 data used in this study were acquired on August 30, 2004 by Milan–Flug over the Schönbrunn area of Vienna. The study area was chosen to comprise a large variety of land cover types, including the buildings and park of Schloß

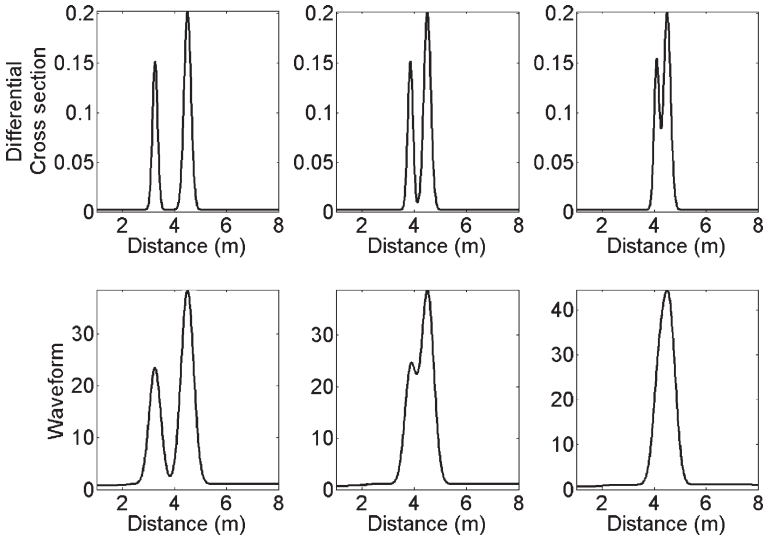

Fig. 6. Illustration of the effect of clustered scatterers on the shape of the observed waveform. The top row shows the assumed differential cross-section of two scatterers separated by a distance larger (left), comparable (middle), and smaller (right) than the range resolution of the airborne laser scanner. The bottom row shows the resulting waveforms.

Schönbrunn, densely built-up areas, residential areas and allotment gardens. Even natural forest is present in the southern part of the Schloß Schönbrunn park. Flight altitude was about 500 m above ground, which resulted in a laser footprint size of 25 cm on ground. An area of about 2 km^2 was covered by eleven parallel flight tracks. The scan rate was set to 66 kHz that resulted in a mean point density of four measurements per square meter. For reference, airborne imagery and other GIS data were available.

Although no calibration targets were deployed during the flight campaign, we calibrated the LMS-Q560 data with an external reference target to obtain at least a rough estimate of the backscatter cross-section. For calibration we used an asphalt street and assumed that it behaves like an ideal Lambertian scatterer with a reflectivity of $\rho=0.2$. Under these assumptions the theoretical cross-section of the asphalt road is (Jelalian, 1992):

$$\sigma_{\text{asphalt}} = 0.2\pi R^2 \beta_t^2 \tag{24}$$

We can now use the calibration Eq. (22) to obtain an estimate of the calibration constant:

$$C_{\text{cal}} = \frac{0.2\pi\beta_t^2}{R^2 \hat{P}_{\text{asphalt}} s_{\text{p,asphalt}}} \tag{25}$$

where $\hat{P}_{\text{asphalt}}$ and $s_{\text{p,asphalt}}$ are the observed values over the selected reference area. This calibration procedure has the advantage that the units, with which the waveform amplitude data are recorded, do not need to be known exactly. Only the linearity criterion needs to be fulfilled, i.e., the recorded signal must be linearly related to the receiver power $P_r(t)$.

5. Results and discussion

We applied the Gaussian decomposition method to all LMS-Q560 data from the eleven flight tracks over the Schönbrunn area. In total more than 26 million waveform profiles were processed. For about 0.9% of all laser shots no echo pulses were registered. This means that either the laser pulse was scattered away from the sensor by a target with a relatively smooth surface or that the surface reflectivity was too low to elevate the echo signal above the noise level. This was mostly the case for water pools within the park area of Schloß Schönbrunn.

For the rest of the data the fitting of the Gaussian pulses was successful for about 98% of waveform profiles. Of those, 86.96% showed only one echo pulse, 11.61% two echoes, 1.35% three echoes, and 0.08% more than three echoes. Up to seven pulses were observed. The root mean square error (RMSE) and the relative RMSE are shown in Fig. 7. The RMSE increases slightly from low to high amplitudes. At small amplitudes the error is determined by the noise of the data. With increasing amplitude the error increases above the noise level because the real system waveform slightly deviates from an ideal Gaussian pulse (Fig. 3). Anyway, as the plot of the relative RMSE versus the amplitude shows, estimates of the pulse properties are much more problematic at small amplitudes where

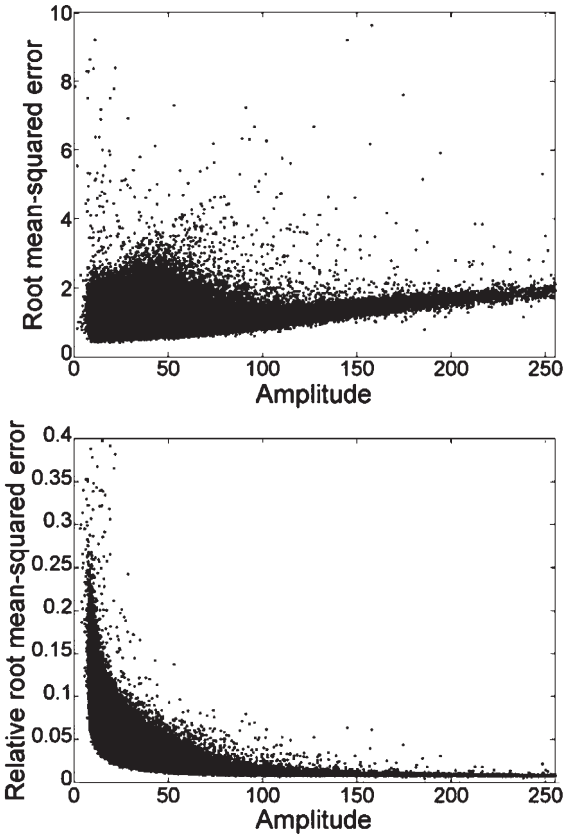

Fig. 7. Root mean square error (top) and relative root mean square error (bottom) versus amplitude for unimodal waveforms.

relative RMSE values higher than 20% can occur. With increasing echo strength the relative RMSE saturates at about 1%. In other words, Gaussian decomposition is robust for strong echoes and may be problematic for weak echoes. This is also illustrated in Fig. 8 that shows a plot of the pulse width versus the amplitude for flat, non-tilted surfaces. While pulse width estimates are relatively stable at high amplitudes, there is significant scattering at low amplitudes. This needs to be taken into account when amplitude and pulse width are used for segmentation and classification purposes.

In a few percent of all cases (2.07%) our criteria indicated that the simple Gaussian pulse model is not appropriate for modelling complex waveforms (Table 3). In a large majority of these cases, the two pulse detection methods did not yield consistent initial estimates of the position of the echo pulses. It also happened in 0.024% of the cases that the initial and fitted pulses were too far apart. However, we attribute these inconsistencies mostly to shortcomings of the pulse detectors and the fitting procedure, combined with a low signal to noise ratio for multiple echo pulses. There is little indication that the real waveform could not be brought in agreement with the simple multiple-pulse model with more tolerant fitting procedures. Nevertheless, the next two situations as indicated in the last two columns of Table 3 clearly represent a problem. In the first one, the unconstrained fitting procedure found echoes with negative amplitude. In the second case the fitting procedure found no solution at all. Anyway, only about 0.03% of the data were affected in this way. This shows that, overall, the assumption of multiple Gaussian pulses is applicable for LMS-Q560 data.

The results of the calibration are shown in Fig. 9 for a small residential area. To illustrate the impact of the different parameters on the backscatter cross-section σ, also plots of the range R, amplitude $\hat{P}$ and pulse width s_p are shown. Visually, it can be observed that the amplitude is responsible for most of the spatial variation of σ, but also variations in range and pulse width are important. For example, pulse width is generally larger for trees compared to meadows. Therefore the effect of the calibration is to make σ of trees more similar to σ of meadows (e.g., regard the "brightening" of the trees in the centre of the area in the cross-section image compared to the amplitude image). The effect of the range is important for large buildings or trees and variations in terrain height (e.g., compare the appearance of the tall, star-like building in the lower-left corner of the area in the amplitude and the cross-section images).

6. Conclusions

Full-waveform airborne laser scanning has recently received increasing attention in the scientific

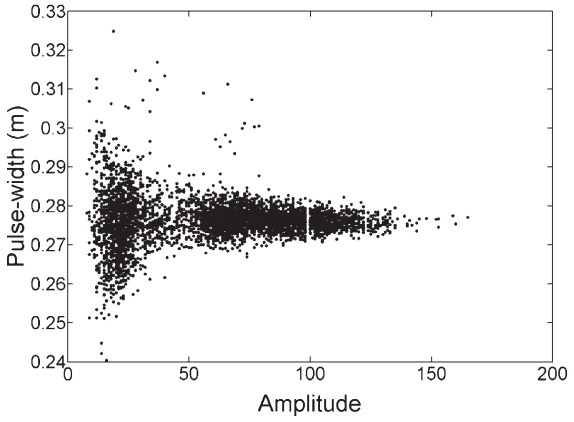

Fig. 8. Estimated pulse width versus pulse amplitude for waveform data from flat, non-tilted surfaces (roads, meadows, flat roofs).

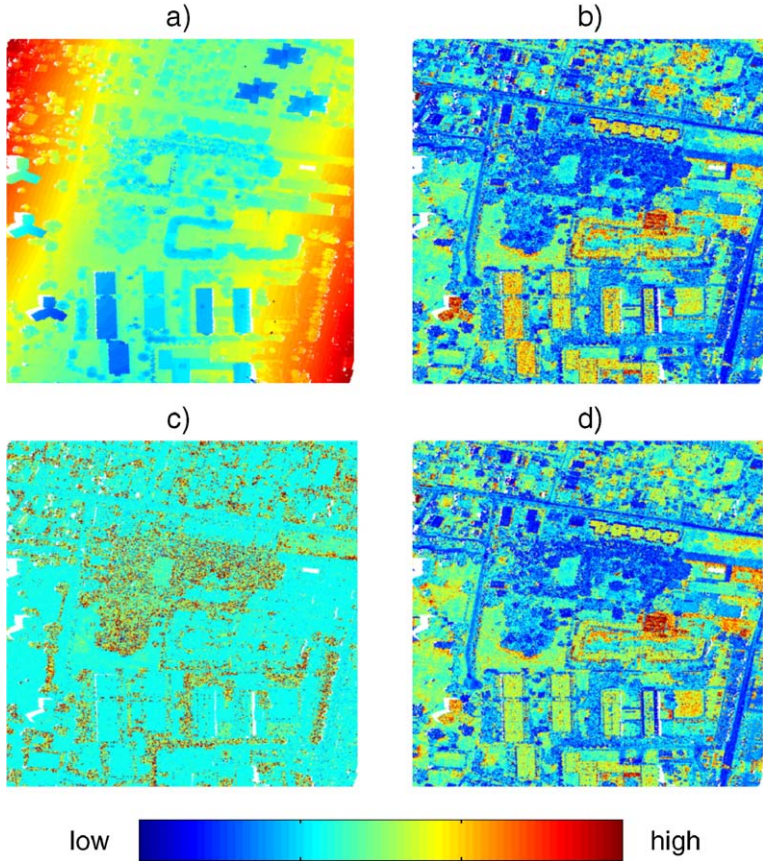

Fig. 9. Calibration of LMS-Q560 data. (a) Range; (b) amplitude; (c) pulse width; and (d) backscatter cross-section.

community. But, as noted by Kim et al. (2003) for forestry applications, we do not yet have a good theoretical understanding of the waveform response for different targets. In this paper we provided a theory for Gaussian pulse formation as a basis for Gaussian decomposition of ALS waveforms, which is currently the most widely applied processing approach. These theoretical considerations also lay the basis for calibrating full-waveform data to obtain estimates of the backscatter cross-section. The algorithms were applied to full-waveform data acquired with the RIEGL LMS-Q560, which is one of the first small-footprint ALS

Table 3
Results of Gaussian decomposition of LMS-Q560 data

Flight track	No. laser shots	Gaussian fitting OK (%)	Initial pulse detectors do not agree (%)	Initial and fitted pulse too far apart (%)	Fitted amplitude is negative (%)	NaN among fitted parameters (%)
1	1915059	98.12	1.82	0.021	0.0385	$4.70\ 10^{-4}$
2	2024159	97.84	2.09	0.027	0.0428	$2.47\ 10^{-4}$
3	2632520	98.10	1.85	0.022	0.0279	$1.14\ 10^{-4}$
4	2573560	97.80	2.14	0.027	0.0326	$4.27\ 10^{-4}$
5	2069241	97.78	2.17	0.028	0.0218	$2.41\ 10^{-4}$
6	2915119	98.06	1.89	0.023	0.0269	$1.09\ 10^{-4}$
7	2108920	97.99	1.96	0.03	0.0197	$2.85\ 10^{-4}$
8	2690600	98.05	1.89	0.023	0.0368	$2.23\ 10^{-4}$
9	2083840	98.04	1.90	0.023	0.0369	$9.60\ 10^{-5}$
10	2563000	98.07	1.87	0.024	0.0358	$1.56\ 10^{-4}$
11	2789937	98.37	1.58	0.018	0.0319	$1.43\ 10^{-4}$
Mean	2396905	97.93	1.92	0.024	0.0320	$2.28\ 10^{-4}$

systems capable of digitising the complete waveform. It was found that, in general, the small-footprint waveform data can indeed be reasonably well modelled by a series of Gaussian pulses. In only 2% of all waveforms our strict criteria indicated more complex, non-Gaussian pulses. This does not necessarily prove that the true cross-section profile normally resembles a series of Gaussian pulses quite well. In many cases, such as vegetation canopies or complex man-made structure, one must even expect substantial variations of the cross-section over distances shorter than the range resolution of ALS system, which is currently in the order of 0.6–1.5 m. This system-inherent limitation should be kept in mind when interpreting the data over such complex targets. Nevertheless, the amplitude, pulse width, and cross-section data derived over our test site in Vienna indicate a large potential for segmentation and classification purposes. So far, ALS systems have provided only 3D coordinates, which meant that segmentation and classification approaches had to rely on geometric information only. Now, each point is characterised, in addition to its position in 3D space, by the amplitude, width and cross-section. This combination of geometric and thematic information is expected to trigger unforeseen possibilities in 3D segmentation and classification.

Acknowledgements

We would like to thank the Schloß Schönbrunn Kultur-und Betriebsges.m.b.H for their support of the data acquisition campaign. Also we would like to thank all colleagues from TU Wien and RIEGL who have been involved in carrying out the field campaign and processing of the data, foremost Dr. Helmut Kager for solving the challenging task of georeferencing the laser scanner data.

References

Abshire, J.B., Xiaoli, S., Afzal, R.S., 2000. Mars Orbiter Laser Altimeter: receiver model and performance analysis. Applied Optics 39 (15), 2449–2460.

Axelsson, P., 1999. Processing of laser scanner data—algorithms and applications. ISPRS Journal of Photogrammetry and Remote Sensing 54 (2–3), 138–147.

Baltsavias, E.P., 1999. Airborne laser scanning: existing systems and firms and other resources. ISPRS Journal of Photogrammetry and Remote Sensing 54 (2–3), 164–198.

Bennia, A., Sedki, M.R., 1990. An optimization technique for iterative frequency-domain deconvolution. IEEE Transactions on Instrumentation and Measurement 39 (2), 358–362.

Blair, J.B., Coyle, D.B., Bufton, J.L., Harding, D.J., 1994. Optimization of an airborne laser altimeter for remote sensing of vegetation and tree canopies. Geoscience and Remote Sensing Symposium (IGARSS '94), vol. 2, pp. 939–941.

Blair, J.B., Rabine, D.L., Hofton, M.A., 1999. The Laser Vegetation Imaging Sensor: a medium-altitude, digitisation-only, airborne laser altimeter for mapping vegetation and topography. ISPRS Journal of Photogrammetry and Remote Sensing 54 (2–3), 115–122.

Cherkassky, V., Mulier, F., 1998. Learning from Data. Wiley.

Flood, M., 2001. Laser altimetry: from science to commercial lidar mapping. Photogrammetric Engineering and Remote Sensing 67 (11), 1209–1217.

Girosi, F., Jones, M., Poggio, T., 1995. Regularization theory and neural networks architectures. Neural Computation 7 (2), 219–269.

Harding, D.J., Lefsky, M.A., Parker, G.G., Blair, J.B., 2001. Laser altimeter canopy height profiles: methods and validation for closed-canopy, broadleaf forest. Remote Sensing of Environment 76 (3), 283–297.

Hofton, M.A., Minster, J.B., Blair, J.B., 2000. Decomposition of laser altimeter waveforms. IEEE Transactions on Geoscience and Remote Sensing 38 (4), 1989–1996.

Hofton, M.A., Rocchio, L.E., Blair, J.B., Dubayah, R., 2002. Validation of vegetation canopy lidar sub-canopy topography measurements for a dense tropical forest. Journal of Geodynamics 34 (3–4), 491–502.

Hug, C., Ullrich, A., Grimm, A., 2004. LITEMAPPER-5600—a waveform digitising lidar terrain and vegetation mapping system. International Archives of Photogrammetry, Remote Sensing and Spatial Information Sciences 36, 24–29 (Part 8/W2).

Jutzi, B., Stilla, U., 2003. Laser pulse analysis for reconstructing and classification of urban objects. International Archives of Photogrammetry, Remote Sensing and Spatial Information Sciences 34, 151–156 (Part 3/W8).

Jelalian, A.V., 1992. Laser Radar Systems. Artech House, Boston London.

Kaasalainen, S., Ahokas, E., Hyyppä, J., Suomalainen, J., 2005. Study of surface brightness from backscattered intensity: calibration of laser data. IEEE Geoscience and Remote Sensing Letters 2 (3), 255–259.

Katzenbeisser, R., Kurz, S., 2004. Airborne Laser-Scanning, ein Vergleich mit terrestrischer Vermessung und Photogrammetrie. Photogrammetrie, Fernerkundung, Geoinformation 3/2004, 179–187.

Kim, K., Treitz, P., Wulder, M., Benoît, St.-O., Flood, M., 2003. LiDAR remote sensing of forest structure. Progress in Physical Geography 27 (1), 88–106.

Persson, Å., Söderman, U., Töpel, J., Ahlberg, S., 2005. Visualization and analysis of full-waveform airborne laser scanner data. International Archives of Photogrammetry, Remote Sensing and Spatial Information Sciences 36, 103–108 (Part 3/W19).

Rottensteiner, F., Trinder, J., Clode, S., Kubik, K., 2005. Using the Dempster Shafer method for the fusion of LIDAR data and multi-spectral images for building detection. Information Fusion 6 (4), 283–300.

Sithole, G., Vosselman, G., 2004. Experimental comparison of filter algorithms for bare-Earth extraction from airborne laser scanning point clouds. ISPRS Journal of Photogrammetry and Remote Sensing 59 (1–2), 85–101.

Ulaby, F.T., Moore, R.K., Fung, A.K., 1982. Microwave remote sensing. Active and Passive. Radar Remote Sensing and Surface Scattering and Emission Theory, vol. II. Artech House Inc., Norwood.

Wagner, W., Ullrich, A., Melzer, T., Briese, C., Kraus, K., 2004. From single-pulse to full-waveform airborne laser scanners: potential and practical challenges. International Archives of Photogrammetry, Remote Sensing and Spatial Information Sciences 35, 201–206 (Part B3).

Zwally, H.J., Schutz, B., Abdalati, W., Abshire, J., Bentley, C., Brenner, A., Bufton, J., Dezio, J., Hancock, D., Harding, D., Herring, T., Minster, B., Quinn, K., Palm, S., Spinhirne, J., Thomas, R., 2002. ICESat's laser measurements of polar ice, atmosphere, ocean, and land. Journal of Geodynamics 34 (3–4), 405–445.